

Quantum Confinement Induced Metal-Insulator Transition in Strongly Correlated Quantum Wells of SrVO_3 Superlattices

A. D. N. James,¹ M. Aichhorn,² and J. Laverock¹

¹*H. H. Wills Physics Laboratory, University of Bristol, Tyndall Avenue, Bristol, BS8 1TL, United Kingdom*

²*Institute of Theoretical and Computational Physics, TU Graz, NAWI Graz, Petersgasse 16, 8010 Graz, Austria*

(Dated: October 6, 2021)

Dynamical mean-field theory (DMFT) has been employed in conjunction with density functional theory (DFT+DMFT) to investigate the metal-insulator transition (MIT) of strongly correlated $3d$ electrons due to quantum confinement. We shed new light on the microscopic mechanism of the MIT and previously reported anomalous subband mass enhancement, both of which arise as a direct consequence of the quantization of $V\ xz(yz)$ states in the SrVO_3 layers. We therefore show that quantum confinement can sensitively tune the strength of electron correlations, leading the way to applying such approaches in other correlated materials.

In strongly correlated quantum materials, the interaction energy between electrons is comparable to their kinetic energy, leading to many-body behavior and the emergence of qualitatively new phenomena [1]. For example, transition metal oxides host properties as diverse as colossal magnetoresistance, high-temperature superconductivity, and Mott insulating phases, each of which have huge potential for future device and technology applications [2, 3]. More recently, substantial advances in the quality and control of layer-by-layer growth methods have facilitated designed transition metal oxide heterostructures and superlattices (SL), often focusing on emergence at interfaces and/or surfaces [4]. Here, we show that correlated electronic behavior may be delicately tuned by quantum confinement, which narrows the effective bandwidth of the correlated quantum well (QW) subbands, and establishes another means to tune physical properties to suit applications. We illustrate this by driving the prototypical correlated metal, SrVO_3 , through a metal-insulator transition (MIT) to a Mott insulating phase, in excellent quantitative agreement with the experimental spectral function extracted from recent spectroscopic measurements [5].

In the bulk, SrVO_3 is a well-characterized correlated metal [6]. Sharp $3d$ quasiparticle (QP) bands at low excitation energies lead to a well-defined Fermi surface [7], while localized states form incoherent Hubbard sidebands at an energy scale comparable with the Coulomb repulsion parameter, U [8, 9]. Together, these yield the familiar three-peaked spectral function [3, 10]. While density functional theory (DFT) often adequately describes QP states (once renormalization is accounted for), it is not capable of capturing the many-body behavior, e.g. Hubbard sidebands are completely absent. Dynamical mean-field theory (DMFT), on the other hand, is able to describe all of the on-site local correlations [3, 10], and has been well-tested on SrVO_3 with very good results, including the energetics and spectral weight of Hubbard sidebands and QP renormalization [3, 8, 11, 12].

The importance of electron correlations in a system may be gauged in terms of the ratio, U/W , where W is the bandwidth. This ratio is known to be significantly enhanced at the SrVO_3 surface [13, 14], and in few layer systems [15, 16]. However, such systems have reduced coordination at the surface,

which is often complicated by reconstruction and relaxation [14]. For example, an insulating phase has been observed in SrVO_3 thin films for thicknesses below approximately 6 unit cells, which was attributed to dimensional crossover due to reduced coordination [15, 17]. In bilayer SrVO_3 , a DFT+DMFT study has established that a Mott insulator emerges due to crystal field (CF) effects [16]; similar CF-induced insulating phases are predicted in other vanadates [18–21]. Although QW structures are well-known in semiconducting [22] and free electron-like [23] materials, their application to correlated $3d$ metals has only recently been realized in a select few transition metal oxides [24, 25], including in few-layer SrVO_3 thin films [26]. However, the precise nature of these states, including their unusual subband renormalization [26, 27], is not yet well understood, although this is essential in order to exploit their properties.

In this Letter, we show that quantum confinement can be employed to precisely control strongly correlated electron behavior. We reveal the microscopic mechanism involved using a combination of DFT, DFT+DMFT and tight-binding models applied to the prototypical correlated oxide SrVO_3 , which we embed within layers of SrTiO_3 in a SL for direct comparison with previous experimental results [5]. Our results accurately reproduce the trends of the experimental data, and reveal that the microscopic mechanism for the MIT in $\text{SrVO}_3/\text{SrTiO}_3$ SLs is due to quantum confinement. Our results also shed light on previous observations of anomalous mass enhancement in SrVO_3 QWs [26, 27], which can be naturally explained as consequences of quantization. These results underline the efficacy of SL engineering in tuning strongly correlated behavior, and leads the way to harnessing functional correlated electron properties in other materials [28].

DFT calculations were performed using the all-electron full potential augmented plane wave ELK package [29] within the local density approximation (LDA). The results are in excellent agreement with previous pseudopotential calculations [5]. The structures of the $(\text{SrVO}_3)_p/(\text{SrTiO}_3)_q$ SLs are shown in Fig. 1(a) for the three SLs investigated here, with $p:q = 2:7, 3:6$ and $6:5$. These were chosen for direct comparison with previous experimental results [5, 30]. Experimental lattice parameters were used: the in-plane parameters

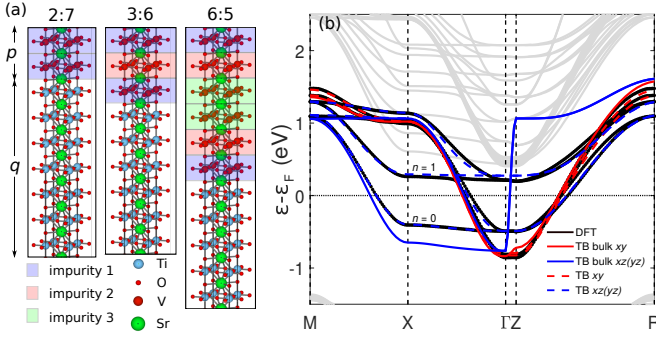


FIG. 1. (a) Schematic diagram of the SL structures, where p and q represent the number of SrVO_3 and SrTiO_3 layers, respectively. The SL unit cells used in the DFT are indicated by the black boxes. The color coded layers illustrate the impurities used in the DMFT calculation. (b) Quantized tight-binding bands for the 2:7 SL. The colored dashed lines indicate the intrinsic bulk bands from which the quantized bands are derived (see text). The discrete energies from the DFT calculation are shown for comparison (both V and Ti t_{2g} bands are given). The grey bands are non-V t_{2g} .

were those of the $(\text{LaAlO}_3)_{0.3}(\text{Sr}_2\text{TaAlO}_6)_{0.7}$ (LSAT) substrate, $a = b = 3.868 \text{ \AA}$, and out-of-plane parameters were $c_{2:7} = 4.00 \text{ \AA}$, $c_{3:6} = 3.97 \text{ \AA}$ and $c_{6:5} = 3.92 \text{ \AA}$. Even in the absence of the SL heterostructure, the different in- and out-of-plane lattice parameters weakly break the V t_{2g} degeneracy into $3d_{xy}$ and $xz(yz)$ orbitals.

In order to interpret our results, the LDA results for each SL were parameterized using a quantized Bohr-Sommerfeld tight-binding (QTB) model [23, 31]. In this model, the *shape* of the TB bands was fixed to that of bulk SrVO_3 , and the free parameters represent the band centers, bandwidths and quantization parameters. In this way, CF splitting and band narrowing between xy and $xz(yz)$ orbitals can be fully captured. The results of fitting this model to the full ELK calculation is shown in Fig. 1(b) for the 2:7 SL, demonstrating the excellent agreement between the two. The quantized nature of the V $xz(yz)$ orbitals is clearly evident, leading to two sub-bands ($n = 0, 1$) originating from the two SrVO_3 layers. In Fig. 1(b), we also show the “intrinsic” TB bands, which correspond to bulk-like bands before the quantization conditions are applied and represent the intrinsic 3D electronic structure from which the QW states emerge.

For the DMFT calculation, the TRIQS/CTHYB continuous-time quantum Monte Carlo (CTQMC) solver [32] and the TRIQS library [33] were used with the Hubbard–Kanamori interaction Hamiltonian, $\beta = 40 \text{ eV}^{-1}$ (290 K), $J = 0.75 \text{ eV}$ and the fully localized limit double counting term, as used previously [16, 18, 19]. The DMFT cycle requires multiple impurities depending on the SL structure, as illustrated schematically in Fig. 1(a). The systems investigated correspond to a single impurity for the 2:7 SL and bulk calculations, and two and three impurities for the 3:6 and 6:5 SLs, respectively. In each case, the impurities are considered to be independent of one another. Only the V t_{2g} bands were projected (using Wannier projectors) to

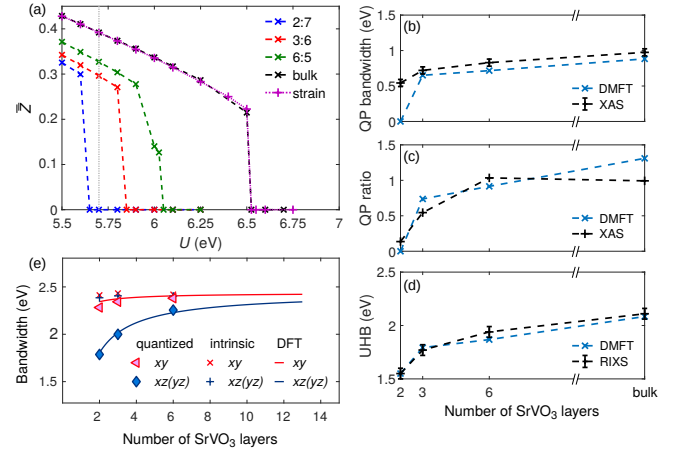


FIG. 2. (a) The orbitally-averaged QP residue, \bar{Z} , for each of the $p:q$ SLs. Also shown are the results of bulk and 1% strained calculations (see text). The grey dotted line indicates the value of $U = 5.7 \text{ eV}$ used for subsequent calculations. (b-d) Comparison with experimental quantities from x-ray absorption spectroscopy (XAS) and resonant inelastic x-ray scattering (RIXS) data [5, 31]; (b) QP bandwidth; (c) Spectral weight within QP states compared with upper Hubbard band states (UHB); (d) Energy of UHB (the DMFT results have been rigidly shifted to match at the 2:7 SL). (e) The bandwidths of the SLs from the DFT calculation and QTB model. Also shown are the intrinsic (bulk) bandwidths of the QTB model.

construct the LDA Hamiltonian in Wannier space to be used in the DMFT calculation [34]. The results presented use the fully charge self-consistent DFT+DMFT technique as implemented in the TRIQS/DFTTools library [35]. We obtain similar results with the one-shot approach with the exception of the orbital charges [31], which is consistent with other studies [18–20]. For each SL structure, U was varied in the range 5.5 to 6.25 eV, and U_{MIT} was located, corresponding to the U at which the SL becomes insulating. In Fig. 2(a), we show the orbitally-averaged QP residue, $\bar{Z} = (\sum_i Z_i)/N$, for each SL, showing how U_{MIT} increases by $\sim 0.2 \text{ eV}$ for each SL. Here, Z_i was determined from the i th orbital self-energy on the Matsubara frequency axis.

We begin by ensuring that our DFT+DMFT calculations accurately describe the experimental system. In Figs. 2(b-d), we compare quantities extracted from x-ray absorption spectroscopy (XAS) and resonant inelastic x-ray scattering (RIXS) experiments [5] with the corresponding theoretical quantities from our DFT+DMFT calculations for $U = 5.7 \text{ eV}$, chosen to reproduce the phenomenological behavior of the experiments. As demonstrated by Figs. 2(b-d), our DFT+DMFT calculations not only capture the qualitative behavior, but also yield excellent quantitative agreement with the experiment trends. We note that, although the 2:7 SL is macroscopically insulating, it has a small QP spectral weight in the spectroscopic experiments due to properties of the sample.

Insight into the microscopic mechanism for the MIT can be obtained by analyzing the QTB model for each SL. In Fig. 2(e), the bandwidths of the SLs from the DFT calculations

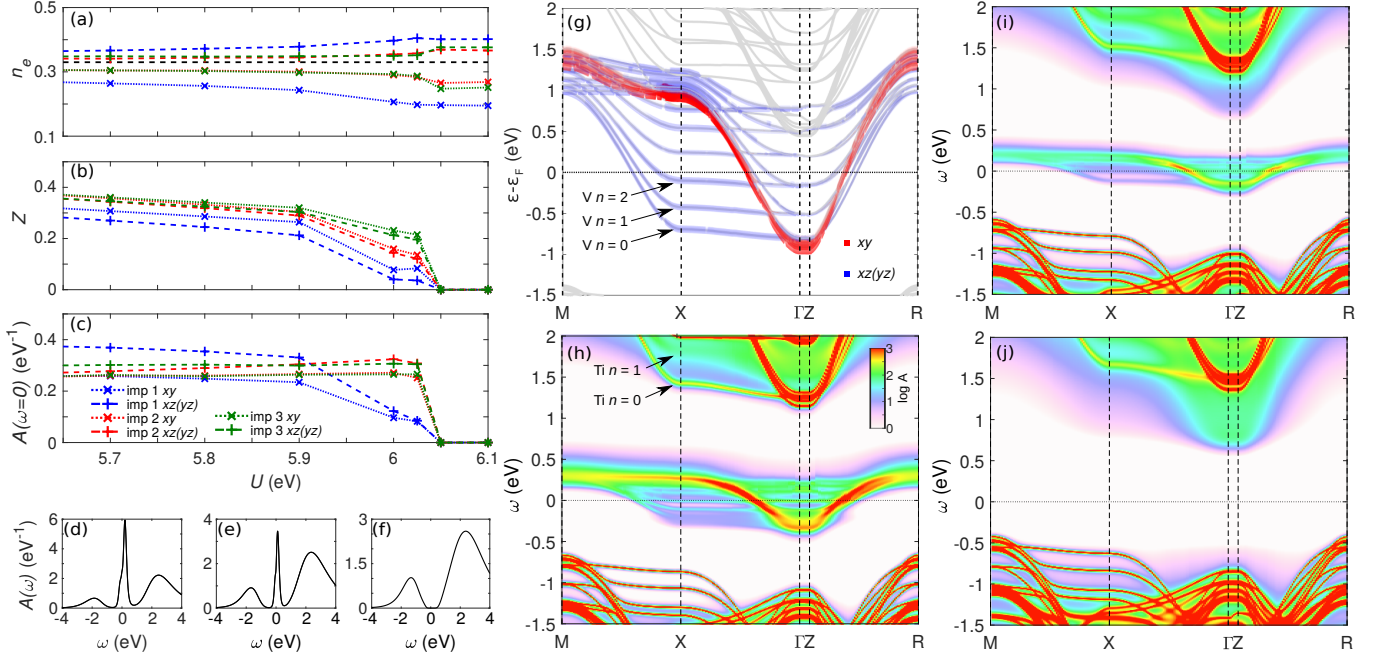


FIG. 3. Correlated QW electronic structure. (a) Occupation number, n_e , (b) QP residue, Z , and (c) spectral function at the Fermi level ($A(\omega = 0)$) of all impurity (imp) correlated orbitals from DFT+DMFT across the MIT for the 6:5 SL. (d-f) The momentum-integrated $V t_{2g}$ spectral function, $A(\omega)$, for $U = 5.7, 6.025$ and 6.05 eV respectively. (g) DFT bandstructure of the 6:5 SL, with $V t_{2g}$ band characters shown. (h) DFT+DMFT momentum-resolved spectral function, $A(\mathbf{k}, \omega)$, of the 6:5 SL for $U = 5.7$ eV, showing directly the renormalization of the correlated bands. (i-j) DFT+DMFT spectral function close to the MIT for $U = 6.025$ and 6.05 eV, respectively.

are shown alongside those from the QTB model. While the in-plane xy orbitals experience a slight narrowing for thinner SrVO_3 SLs, the overall band narrowing of the (quantized) out-of-plane $xz(yz)$ orbitals is substantial, leading to a bandwidth reduction of $\sim 70\%$ for the 2:7 SL [5]. As expected from the quality of the fits in Fig. 1(b), good agreement is observed between the QTB and DFT results. However, this behavior is not captured at all by the “intrinsic” bandwidths, which correspond to the effective 3D bands of the QTB model before quantization. These results demonstrate that the band narrowing in Fig. 2(e) is due to quantization of the $xz(yz)$ orbitals, which has a more pronounced impact for thinner SrVO_3 layers. The band narrowing of the thinner SLs leads to a greater U/W ratio, which results in stabilization of the insulating phase, as illustrated by the DFT+DMFT calculations shown in Fig. 2(a).

A previous DMFT study has attributed CF effects as being the principle factor driving the MIT in bilayer SrVO_3 on SrTiO_3 [16], and it is pertinent to ask what role, if any, the CF plays in our system. In Ref. 16, strain induced by the SrTiO_3 substrate led to a lowering of the xy orbitals by 180 meV due to the CF. In contrast, we find a CF splitting of ≤ 51 meV in favor of the $V xz(yz)$ bands in our SLs, in part owing to the lower strain imparted by the LSAT substrate. To reproduce the effects of this CF, we have calculated strained SrVO_3 with a volume-conserving strain of 1%, which leads to similar CF splitting of 53 meV [31]. This 3D system, which reproduces the CF levels of our SLs but without the quantization effects,

is shown in Fig. 2(a), and shows very similar behavior to the bulk cubic system. Therefore, we confidently rule out CF effects as a dominant factor in our SLs.

Finally, we discuss the correlated behavior of the quantized electron states, taking the 6:5 SL as an example. Figure 3(a-c) shows the orbital- and layer-resolved occupation number, n_e , QP residue, Z , and spectral weight at the Fermi level, $A(\omega = 0)$, as a function of U , illustrating the transition to the insulating phase at $U = 6.05$ eV for this SL. As presented in Fig. 3(a), each layer (impurity) exhibits a sizeable orbital polarization in favor of the xy orbitals, which is exaggerated both at the outer (interface) layer and in the insulating phase. This behavior is consistent across all SLs, and originates from a small polarization in the DFT calculations due to the local CF, which is subsequently amplified in the DMFT cycle [31]. The outer layer (impurity 1) is significantly “more correlated”, experiencing a smaller QP residue Z than the other layers [Fig. 3(b)], corresponding to a greater renormalization factor, $1/Z$. Near the MIT, this leads to a collapse in the spectral weight at $\omega = 0$ of the interface layer [Fig. 3(c)]. In this sense, the more correlated interface layer simultaneously triggers the MIT in the remaining layers, in much the same way as suggested for SrVO_3 bilayers in Ref. 16.

The DMFT spectral functions, $A(\omega)$ and $A(\mathbf{k}, \omega)$, are shown in Fig. 3(d-f) and Fig. 3(h-j) for $U = 5.7, 6.025$ and 6.05 eV, respectively, and were calculated using the maximum entropy method within TRIQS [36]. The renormalization of the V bands increases from a factor of $1/\bar{Z} \approx 3.5$ at

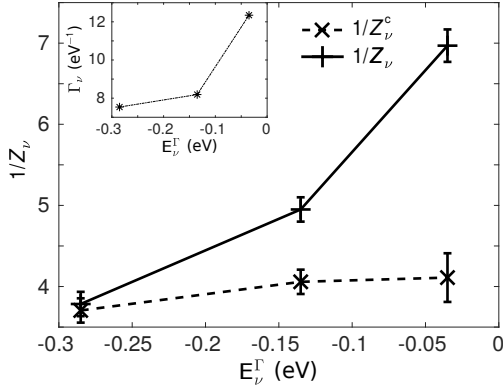


FIG. 4. The total mass enhancement factor of each subband, $1/Z_\nu$, of the 6:5 SL at $U = 5.7$ eV shown alongside the correlation-only mass enhancement factor $1/Z_\nu^c$, evaluated along X - M . The abscissa represents the bottom energy of the subband. Error bars indicate the estimated error in determining these quantities. The inset shows the subband lifetime Γ_ν . All lines are guides to the eye.

$U = 5.7$ eV to ≈ 8 just below the MIT ($U = 6.05$ eV) before the QP spectral weight vanishes in the insulating phase [Fig. 3(f)]. The renormalization of the V bands is accompanied by a lowering in their energy with respect to O and Ti bands, leading to pronounced energy separation of O/Ti bands and metallic V t_{2g} QPs. Nevertheless, the quantized subband structure remains clear in the metallic solutions, leading to genuinely strongly correlated QWs. At $U = 5.7$ eV, the lowest three yz subbands are occupied at X and Γ , similar to the DFT, however by $U = 6.025$ eV only the lowest subband is occupied, indicating the quantized system undergoes a correlation-induced Lifshitz transition prior to the MIT. Although the correlated orbitals remain relatively sharp throughout near $\omega = 0$, implying long-lived QPs with a well-defined Fermi surface, the lifetime rapidly broadens away from ε_F , in line with a strongly correlated Fermi liquid (see inset to Fig. 4). We also note that the incoherent upper Hubbard band (UHB), visible above 1 eV in [Fig. 3(j)], exhibits rather strong momentum dependence, visible in previous bulk DMFT calculations [11, 37]. Unexpectedly, certain (uncorrelated) Ti states also show pronounced broadening, e.g. the $n = 1$ Ti yz orbital indicated in Fig. 3(h), which is almost completely smeared out at $U = 6.025$ eV [Fig. 3(i)]. This arises due to the spatial penetration of the Ti wavefunctions at the interface into the correlated SrVO₃ layers, leading to broadening of those subbands that have significant weight at the interface [31]. This surprising sensitivity of the Ti states may help to explain recent RIXS results of the SrTiO₃ layers of SrVO₃/SrTiO₃ SLs, where a sudden change in the delocalized Ti $3d$ carrier density was observed coincident with the MIT of the SrVO₃ layers [38].

We finish by discussing some important implications of our results. Anomalous mass enhancement has been reported in SrVO₃ QWs, whereby shallower occupied subbands were

found to have a larger mass enhancement ($m^* = m/Z_\nu$) than subbands at deeper energies [26]. Subsequent theoretical [39] and experimental [27] studies argued the anomalous enhancement was a consequence of a combination of electron correlation effects and the reduced dimensionality of the surface. To address this, we compare the total mass enhancement of a particular quantized subband, $1/Z_\nu$, with that due solely to electron correlation, $1/Z_\nu^c$, both of which are obtained through analysis of the Fermi velocities [31]. The trend in the total mass enhancement factor, $1/Z_\nu$, which includes both correlation effects and band effects due to quantization, qualitatively reproduces the experimental data [26] rather well, but this behavior is only very weakly present in $1/Z_\nu^c$. Therefore, in our SLs the origin of the mass enhancement is firmly due to k_z sampling introduced by quantization, as has been observed in other systems [25]. While reduced coordination at the surface [14, 39], surface reconstruction [40], or specific k_z sampling due to an asymmetric phase shift at the vacuum [25, 41] may play additional roles in specific surface-terminated systems, our results reveal quantization as the primary source of anomalous mass enhancement in embedded (or capped) few-layer SrVO₃.

In summary, our results establish quantum confinement engineering as a sensitive method to tune the correlated electron behavior of $3d$ electron systems. We demonstrate our approach using SLs of few-layer SrVO₃ embedded in SrTiO₃: this system exhibits an MIT due to a reduction in bandwidth by varying the number of SrVO₃ layers. The microscopic mechanism we reveal is a direct consequence of quantum confinement, and is distinct from previous studies invoking CF effects [16] or dimensionality [15], demonstrating the excellent versatility of the MIT in SrVO₃ with respect to different control parameters. Similar to Ref. 16, we find that the outer layers at the interface of the quantum well are more strongly correlated, and trigger the transition in the rest of the layer. Our interpretation is also able to naturally explain the anomalous mass enhancement previously reported in ARPES measurements [26, 27]. Together, these results demonstrate the potency of employing quantum confinement as a tuning parameter for correlated electron behavior in engineered SLs. This approach also has the significant benefits that surface effects are avoided and that large (bulk-like) volumes of the system may respond to external stimuli. Aside from the expected improved performance of such a SrVO₃ device as a Mott transistor [16], quantized SLs made of other correlated materials are likely to show improved properties, e.g. superconducting devices in cuprate SLs [42], conductivity in nickelate SLs [43] or spintronic devices [44].

A.D.N.J. acknowledges funding and support from the Engineering and Physical Sciences Research Council (EPSRC) Centre for Doctoral Training in Condensed Matter Physics (CDT-CMP), Grant No. EP/L015544/1. M.A acknowledges financial support from the Austrian Science Fund (FWF), START program Y746. Calculations were performed using the computational facilities of the Advanced Computing Research Centre, University of Bristol (<http://bris.ac.uk/acrc/>).

The authors would like to thank Dr. G. Kraberger and Prof. S. B. Dugdale for their useful discussions and contributions related to this work. The VESTA package (<https://jp-minerals.org/vesta/en/>) has been used in the preparation of some figures.

-
- [1] Y. Tokura, M. Kawasaki, and N. Nagaosa, “Emergent functions of quantum materials,” *Nature Phys.* **13**, 1056 (2017).
 - [2] M. Brahlek, L. Zhang, J. Lapano, H.-T. Zhang, R. Engel-Herbert, N. Shukla, S. Datta, H. Paik, and D.G. Schlom, “Opportunities in vanadium-based strongly correlated electron systems,” *MRS Commun.* **7**, 27 (2017); J. Mannhart and D. G. Schlom, “Oxide interfaces — an opportunity for electronics,” *Science* **327**, 1607 (2010).
 - [3] G. Kotliar, S. Y. Savrasov, K. Haule, V. S. Oudovenko, O. Parcollet, and C. A. Marianetti, “Electronic structure calculations with dynamical mean-field theory,” *Rev. Mod. Phys.* **78**, 865 (2006).
 - [4] M. Izumi, Y. Ogimoto, Y. Konishi, T. Manako, M. Kawasaki, and Y. Tokura, “Perovskite superlattices as tailored materials of correlated electrons,” *Mater. Sci. Eng. B* **84**, 53 (2001); A. Ohtomo and H. Y. Hwang, “A high-mobility electron gas at the $\text{LaAlO}_3/\text{SrTiO}_3$ heterointerface,” *Nature* **427**, 423 (2004); H. Y. Hwang, Y. Iwasa, M. Kawasaki, B. Keimer, N. Nagaosa, and Y. Tokura, “Emergent phenomena at oxide interfaces,” *Nature Mater.* **11**, 103 (2012); J. Chakhalian, J. W. Freeland, A. J. Millis, C. Panagopoulos, and J. M. Rondinelli, “Colloquium: Emergent properties in plane view: Strong correlations at oxide interfaces,” *Rev. Mod. Phys.* **86**, 1189–1202 (2014).
 - [5] J. Laverock, M. Gu, V. Jovic, J. W. Lu, S.A. Wolf, R. M. Qiao, W. Yang, and K.E. Smith, “Nano-engineering of electron correlation in oxide superlattices,” *Nano Futures* **1**, 031001 (2017).
 - [6] I. A. Nekrasov, G. Keller, D. E. Kondakov, A. V. Kozhevnikov, Th. Pruschke, K. Held, D. Vollhardt, and V. I. Anisimov, “Comparative study of correlation effects in CaVO_3 and SrVO_3 ,” *Phys. Rev. B* **72**, 155106 (2005).
 - [7] T. Yoshida, M. Hashimoto, T. Takizawa, A. Fujimori, M. Kubota, K. Ono, and H. Eisaki, “Mass renormalization in the bandwidth-controlled mott-hubbard systems SrVO_3 and CaVO_3 studied by angle-resolved photoemission spectroscopy,” *Phys. Rev. B* **82**, 085119 (2010); S. Aizaki, T. Yoshida, K. Yoshimatsu, M. Takizawa, M. Minohara, S. Ideta, A. Fujimori, K. Gupta, P. Mahadevan, K. Horiba, H. Kumigashira, and M. Oshima, “Self-energy on the low-to high-energy electronic structure of correlated metal SrVO_3 ,” *Phys. Rev. Lett.* **109**, 056401 (2012).
 - [8] A. Sekiyama, H. Fujiwara, S. Imada, S. Suga, H. Eisaki, S. I. Uchida, K. Takegahara, H. Harima, Y. Saitoh, I. A. Nekrasov, G. Keller, D. E. Kondakov, A. V. Kozhevnikov, Th. Pruschke, K. Held, D. Vollhardt, and V. I. Anisimov, “Mutual experimental and theoretical validation of bulk photoemission spectra of $\text{Sr}_{1-x}\text{Ca}_x\text{VO}_3$,” *Phys. Rev. Lett.* **93**, 156402 (2004).
 - [9] H. F. Pen, M. Abbate, A. Fujimori, Y. Tokura, H. Eisaki, S. Uchida, and G. A. Sawatzky, “Electronic structure of $\text{Y}_{1-x}\text{Ca}_x\text{VO}_3$ studied by high-energy spectroscopies,” *Phys. Rev. B* **59**, 7422–7432 (1999); J. Laverock, B. Chen, K. E. Smith, R. P. Singh, G. Balakrishnan, M. Gu, J. W. Lu, S. A. Wolf, R. M. Qiao, W. Yang, and J. Adell, “Resonant soft-x-ray emission as a bulk probe of correlated electron behavior in metallic $\text{Sr}_x\text{Ca}_{1-x}\text{VO}_3$,” *Phys. Rev. Lett.* **111**, 047402 (2013).
 - [10] A. Georges, G. Kotliar, W. Krauth, and M. J. Rozenberg, “Dynamical mean-field theory of strongly correlated fermion systems and the limit of infinite dimensions,” *Rev. Mod. Phys.* **68**, 13 (1996).
 - [11] I. A. Nekrasov, K. Held, G. Keller, D. E. Kondakov, Th. Pruschke, M. Kollar, O. K. Andersen, V. I. Anisimov, and D. Vollhardt, “Momentum-resolved spectral functions of SrVO_3 calculated by LDA+DMFT,” *Phys. Rev. B* **73**, 155112 (2006).
 - [12] K. Byczuk, M. Kollar, K. Held, Y.-F. Yang, I. A. Nekrasov, Th. Pruschke, and D. Vollhardt, “Kinks in the dispersion of strongly correlated electrons,” *Nat. Phys.* **3**, 168 (2007); J. M. Tomczak, M. Casula, T. Miyake, F. Aryasetiawan, and S. Biermann, “Combined GW and dynamical mean-field theory: Dynamical screening effects in transition metal oxides,” *Europhys. Lett.* **100**, 67001 (2012).
 - [13] K. Maiti, D. D. Sarma, M. J. Rozenberg, I. H. Inoue, H. Makino, O. Goto, M. Pedio, and R. Cimino, “Electronic structure of $\text{Ca}_{1-x}\text{Sr}_x\text{VO}_3$: A tale of two energy scales,” *EPL (Europhys. Lett.)* **10**, 246 (2001); A. Liebsch, “Surface versus Bulk Coulomb Correlations in Photoemission Spectra of SrVO_3 and CaVO_3 ,” *Phys. Rev. Lett.* **90**, 096401 (2003); J. Laverock, J. Kuyyalil, B. Chen, R. P. Singh, B. Karlin, J. C. Woicik, G. Balakrishnan, and K. E. Smith, “Enhanced electron correlations at the $\text{Sr}_x\text{Ca}_{1-x}\text{VO}_3$ surface,” *Phys. Rev. B* **91**, 165123 (2015).
 - [14] H. Ishida, D. Wortmann, and A. Liebsch, “Electronic structure of $\text{SrVO}_3(001)$ surfaces: A local-density approximation plus dynamical mean-field theory calculation,” *Phys. Rev. B* **73**, 245421 (2006).
 - [15] K. Yoshimatsu, T. Okabe, H. Kumigashira, S. Okamoto, S. Aizaki, A. Fujimori, and M. Oshima, “Dimensional-crossover-driven metal-insulator transition in SrVO_3 ultrathin films,” *Phys. Rev. Lett.* **104**, 147601 (2010).
 - [16] Z. Zhong, M. Wallerberger, J. M. Tomczak, C. Taranto, N. Paragh, A. Toschi, G. Sangiovanni, and K. Held, “Electronics with Correlated Oxides: $\text{SrVO}_3/\text{SrTiO}_3$ as a Mott Transistor,” *Phys. Rev. Lett.* **114**, 246401 (2015).
 - [17] M. Gu, S. A. Wolf, and J. Lu, “Two-dimensional Mott insulators in SrVO_3 ultrathin films,” *Adv. Mater. Interfaces* **1**, 1300126 (2014).
 - [18] S. Bhandary, E. Assmann, M. Aichhorn, and K. Held, “Charge self-consistency in density functional theory combined with dynamical mean field theory: k -space reoccupation and orbital order,” *Phys. Rev. B* **94**, 155131 (2016).
 - [19] M. Schüller, O. E. Peil, G. J. Kraberger, R. Pordzik, M. Marsman, G. Kresse, T. O. Wehling, and M. Aichhorn, “Charge self-consistent many-body corrections using optimized projected localized orbitals,” *J. Phys.: Condens. Matter* **30**, 475901 (2018).
 - [20] A. Hampel, S. Beck, and C. Ederer, “Charge self-consistency and double-counting in DFT+DMFT calculations for complex transition metal oxides,” *arXiv:1907.10339* (2019).
 - [21] S. Beck, G. Sclauzero, U. Chopra, and C. Ederer, “Metal-insulator transition in CaVO_3 thin films: Interplay between epitaxial strain, dimensional confinement, and surface effects,” *Phys. Rev. B* **97**, 075107 (2018); G. Sclauzero, K. Dymkowski, and C. Ederer, “Tuning the metal-insulator transition in d^1 and d^2 perovskites by epitaxial strain: A first-principles-based study,” *Phys. Rev. B* **94**, 245109 (2016).
 - [22] L. Colakerol, T. D. Veal, H.-K. Jeong, L. Plucinski, A. DeMasi, T. Learmonth, P.-A. Glans, S. Wang, Y. Zhang, L. F. J. Piper, P. H. Jefferson, A. Fedorov, T.-C. Chen, T. D. Moustakas, C. F. McConville, and K. E. Smith, “Quantized electron accumulation states in indium nitride studied by angle-resolved photoemission spectroscopy,” *Phys. Rev. Lett.* **97**, 237601 (2006).

- [23] T.-C. Chiang, “Photoemission studies of quantum well states in thin films,” *Surf. Sci. Rep.* **39**, 181 (2000).
- [24] J. Liu, M. Kareev, D. Meyers, B. Gray, P. Ryan, J. W. Freeland, and J. Chakhalian, “Metal-insulator transition and orbital reconstruction in Mott-type quantum wells made of NdNiO_3 ,” *Phys. Rev. Lett.* **109**, 107402 (2012); S. G. Jeong, T. Min, S. Woo, J. Kim, Y.-Q. Zhang, S. W. Cho, J. Son, Y.-M. Kim, J. H. Han, S. Park, H. Y. Jeong, H. Ohta, S. Lee, T. W. Noh, J. Lee, and W. S. Choi, “Phase instability amid dimensional crossover in artificial oxide crystal,” *Phys. Rev. Lett.* **124**, 026401 (2020).
- [25] J. K. Kawasaki, C. H. Kim, J. N. Nelson, S. Crisp, C. J. Zollner, E. Biegenwald, J. T. Heron, C. J. Fennie, D. G. Schlom, and K. M. Shen, “Engineering carrier effective masses in ultrathin quantum wells of IrO_2 ,” *Phys. Rev. Lett.* **121**, 176802 (2018).
- [26] K. Yoshimatsu, K. Horiba, H. Kumigashira, T. Yoshida, A. Fujimori, and M. Oshima, “Metallic quantum well states in artificial structures of strongly correlated oxide,” *Science* **333**, 319 (2011).
- [27] M. Kobayashi, K. Yoshimatsu, E. Sakai, M. Kitamura, K. Horiba, A. Fujimori, and H. Kumigashira, “Origin of the anomalous mass renormalization in metallic quantum well states of strongly correlated oxide SrVO_3 ,” *Phys. Rev. Lett.* **115**, 076801 (2015).
- [28] R. Adler, C.-J. Kang, C.-H. Yee, and G. Kotliar, “Correlated materials design: prospects and challenges,” *Rep. Prog. Phys.* **82**, 012504 (2019).
- [29] J. K. Dewhurst, S. Sharma, L. Nordström, F. Cricchio, O. Granas, and E. K. U. Gross, <http://elk.sourceforge.net/> (2019).
- [30] M. Gu, S. A. Wolf, and J. Lu, “Transport phenomena in $\text{SrVO}_3/\text{SrTiO}_3$ superlattices,” *J. Phys. D: Appl. Phys.* **51**, 10LT01 (2018).
- [31] “Supplementary, [url],” .
- [32] P. Seth, I. Krivenko, M. Ferrero, and O. Parcollet, “TRIQS/CTHYB: A continuous-time quantum monte carlo hybridisation expansion solver for quantum impurity problems,” *Comp. Phys. Commun.* **200**, 274 (2016).
- [33] O. Parcollet, M. Ferrero, T. Ayral, H. Hafermann, I. Krivenko, L. Messio, and P. Seth, “TRIQS: A toolbox for research on interacting quantum systems,” *Comp. Phys. Commun.* **196**, 398 (2015).
- [34] M. Aichhorn, L. Poudrovskii, V. Vildosola, M. Ferrero, O. Parcollet, T. Miyake, A. Georges, and S. Biermann, “Dynamical mean-field theory within an augmented plane-wave framework: Assessing electronic correlations in the iron pnictide LaFeAsO ,” *Phys. Rev. B* **80**, 085101 (2009).
- [35] M. Aichhorn, L. Poudrovskii, and A. Georges, “Importance of electronic correlations for structural and magnetic properties of the iron pnictide superconductor LaFeAsO ,” *Phys. Rev. B* **84**, 054529 (2011); M. Aichhorn, L. Poudrovskii, P. Seth, V. Vildosola, M. Zingl, O. E. Peil, X. Deng, J. Mravlje, G. J. Kraberger, C. Martins, M. Ferrero, and O. Parcollet, “TRIQS/DFTTools: A TRIQS application for ab initio calculations of correlated materials,” *Comp. Phys. Commun.* **204**, 200 (2016).
- [36] G. J. Kraberger and M. Zingl, <https://github.com/TRIQS/maxent> (2019).
- [37] S. Bhandary and K. Held, “Self-energy self-consistent density functional theory plus dynamical mean field theory,” *arXiv:1904.02967v1* (2019).
- [38] J. Laverock, M. Gu, V. Jovic, J. W. Lu, S. A. Wolf, G. Watson, R. M. Qiao, W. Yang, and K. E. Smith, “Electronic reconstructions at the interface of $\text{SrVO}_3/\text{SrTiO}_3$ superlattices,” unpublished (2020).
- [39] S. Okamoto, “Anomalous mass enhancement in strongly correlated quantum wells,” *Phys. Rev. B* **84**, 201305(R) (2011).
- [40] H. Oka, Y. Okada, T. Hitosugi, and T. Fukumura, “Two distinct surface terminations of SrVO_3 (001) ultrathin films as an influential factor on metallicity,” *Appl. Phys. Lett.* **113**, 171601 (2018); G. Wang, Z. Wang, M. Meng, M. Saghayezhian, L. Chen, C. Chen, H. Guo, Y. Zhu, E. W. Plummer, and J. Zhang, “Role of disorder and correlations in the metal-insulator transition in ultrathin SrVO_3 films,” *Phys. Rev. B* **100**, 155114 (2019).
- [41] I. Matsuda, T. Ohta, and H. W. Yeom, “In-plane dispersion of the quantum-well states of the epitaxial silver films on silicon,” *Phys. Rev. B* **65**, 085327 (2002); K. Yoshimatsu, E. Sakai, M. Kobayashi, K. Horiba, T. Yoshida, A. Fujimori, M. Oshima, and H. Kumigashira, “Determination of the surface and interface phase shifts in metallic quantum well structures of perovskite oxides,” *Phys. Rev. B* **88**, 115308 (2013).
- [42] C. H. Ahn, S. Gariglio, P. Paruch, T. Tybell, L. Antognazza, and J.-M. Triscone, “Electrostatic modulation of superconductivity in ultrathin $\text{GdBa}_2\text{Cu}_3\text{O}_{7-x}$ films,” *Science* **284**, 1152 (1999).
- [43] H. Chen, A. J. Millis, and C. A. Marianetti, “Engineering correlation effects via artificially designed oxide superlattices,” *Phys. Rev. Lett.* **111**, 116403 (2013).
- [44] S. Samanta, S. B. Mishra, and B. R. K. Nanda, “Quantum well structure of a double perovskite superlattice and formation of a spin-polarized two-dimensional electron gas,” *Phys. Rev. B* **98**, 115155 (2018).

Supplementary Information for “Quantum Confinement Induced Metal-Insulator Transition in Strongly Correlated Quantum Wells of SrVO₃ Superlattices”

A. D. N. James,¹ M. Aichhorn,² and J. Laverock¹

¹*H. H. Wills Physics Laboratory, University of Bristol, Tyndall Avenue, Bristol, BS8 1TL, United Kingdom*

²*Institute of Theoretical and Computational Physics, TU Graz, NAWI Graz, Petersgasse 16, 8010 Graz, Austria*

(Dated: October 6, 2021)

COMPARISON WITH EXPERIMENTAL QUANTITIES

Figure S1 illustrates the main experimental spectroscopic results on the superlattices (SL) [1, 2], in which transport measurements established that the 2:7 and 3:6 SLs were insulating, whereas the 13:4 SL was metallic. The 6:5 SL was found to be metallic at room temperature, with an metal-insulator transition (MIT) at low temperature. The experimental results (performed at room temperature) show the evolution in correlated electron behavior extracted from x-ray absorption spectroscopy (XAS) and resonant inelastic x-ray scattering (RIXS).

For completeness, we briefly outline the experimental properties and how they were extracted here. The metallicity [Fig. S1(a)] was extracted from both XAS and RIXS as the leading edge of the O *K* edge XAS and from the intensity of the quasi-elastic peak in V *L* edge RIXS. The quasiparticle (QP) bandwidth [Fig. S1(b)] was extracted from the SrVO₃ layer contribution to the O *K* edge XAS as the full-width at half-maximum of the QP peak. The QP spectral weight [Fig. S1(c)] was also extracted from the SrVO₃ layer contribution to the O *K* edge XAS as the ratio of the area under

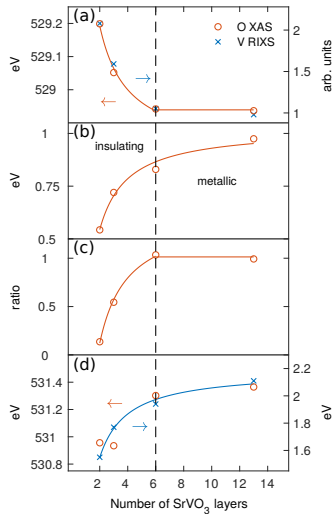


FIG. S1. Evolution of correlated electron behavior from experimental x-ray absorption spectroscopy (XAS) and resonant inelastic x-ray scattering (RIXS) measurements of SrVO₃/SrTiO₃ superlattices, reproduced from Ref. 2. From top to bottom, evolution in (a) metallicity of SLs, (b) quasiparticle (QP) bandwidth, (c) QP spectral weight and (d) the energy of the upper Hubbard band are shown.

the QP peak to the total area under unoccupied V *3d* states (i.e. the sum of QP, upper Hubbard band (UHB) and *e_g* spectral weights). Occupied states are not accessible in O *K* edge XAS. Finally, the UHB energy [Fig. S1(d)] is accessible to both XAS and RIXS. From O *K* edge XAS, the UHB peak is directly observed, and its center is shown here. From V *L* edge RIXS, the UHB energy is available from transitions from occupied QP states to the unoccupied UHB. Both show equivalent evolution with SL structure.

Figure S2 shows a schematic illustration comparing the extracted experimental quantities with their DFT+DMFT (density functional theory with dynamical mean-field theory) definitions. The QP bandwidth has been extracted from the DMFT spectral function by obtaining the width defined by the minima around the central QP peak. The QP ratio was determined by taking the ratio of the quasiparticle weight (labeled *Q* in Fig. S2) and the UHB weight (labeled *U*). Finally, the energy of the UHB was obtained by locating the peak in the DMFT spectral function, referenced to $\omega = 0$. In the experimental RIXS process, the UHB peak energy represents the peak in the joint QP and UHB density of states, and therefore is referenced to an energy $\omega < 0$. To compare the theoretical and experimental quantities, we therefore shift all theoretical quantities to match for the 2:7 SL (the shift is -0.584 eV).

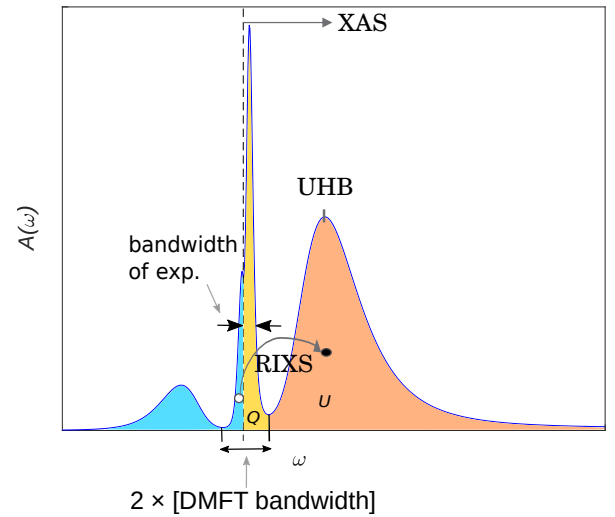


FIG. S2. A schematic illustration showing how the variables in the theory-experimental comparison were determined.

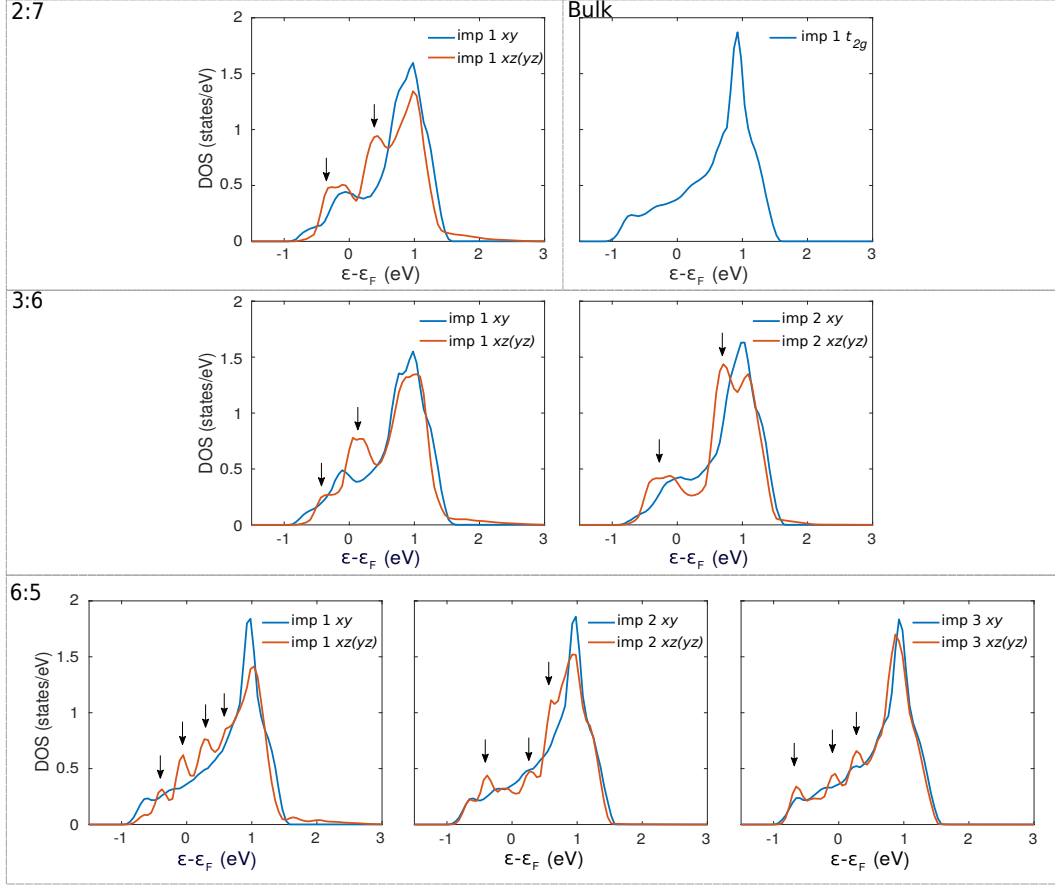


FIG. S3. The DFT $V t_{2g}$ partial density of states (PDOS) of the bulk SrVO_3 , 2:7, 3:6 and 6:5 SLs. The dashed borders outline which plots belong to the corresponding structure. Each panel shows the PDOS of the inequivalent V atoms in each structure, labeled by their impurity number in the DMFT cycles (imp 1 refers to the interface). The arrows indicate the contributions of quantized states to each inequivalent V atom. The greatest contribution are from the relatively flat bands along Γ -X.

DENSITY FUNCTIONAL THEORY CALCULATIONS

DFT calculations were performed using the ELK FP-LAPW (full potential linearized augmented plane wave) code within the local density approximation (LDA) [3]. The results are in excellent agreement with previous pseudopotential calculations within the generalized gradient approximation (GGA) of the same SLs [2]. Previous PES work [4], show how the dimensionality of SrVO_3 influences the MIT. In their results, ten SrVO_3 layers closely resembles bulk behavior. From this, we approximate the 13:4 SL in Ref. 2 with bulk DFT+DMFT calculations.

Self-consistency was achieved on a $12 \times 12 \times 4$ mesh in the full Brillouin zone (BZ) for relatively low computational cost with sufficient sampling, corresponding to 84 k-points in the irreducible ($1/16^{\text{th}}$) BZ. To stabilize the DFT self-consistent cycles, small values of mixing of the new potentials was used, at the cost of computational time. For bulk SrVO_3 , a k-mesh of $12 \times 12 \times 12$ was used (84 k-points in the $1/48^{\text{th}}$ irreducible BZ).

The partial densities of states (PDOS) of t_{2g} orbitals are shown in Fig. S3 for the bulk and 2:7, 3:6 and 6:5 SLs. Sharp peaks in the PDOS reflect the quantized electronic structure along c . For the inner layers of the thicker SLs, the PDOS more closely resembles that of bulk SrVO_3 , e.g. impurity 3 of the 6:5 SL. Near the interface, the $xz(yz)$ PDOS extends to higher energies as a result of mixing of these states with Ti states in the SrTiO_3 layer.

The characters of the subbands are shown in Fig. S4 for each of the different V and Ti sites, using the 6:5 SL as an example. As expected, the V bands dominate the character at the Fermi level, with weak contribution from interfacial Ti ions. The spatial distribution of the subband wavefunctions of the SrVO_3 quantum wells can be seen directly in the characters. The V $n = 0$ subband, with greatest amplitude in the centre of the well, has strong character in the central V ion and weak character at the interface. Correspondingly, the V $n = 2$ subband has strongest character at the interface and is almost absent in the second layer close to where a node is expected in the quantum well wavefunction. At higher energies, the quantized V e_g subbands appear above 1 eV.

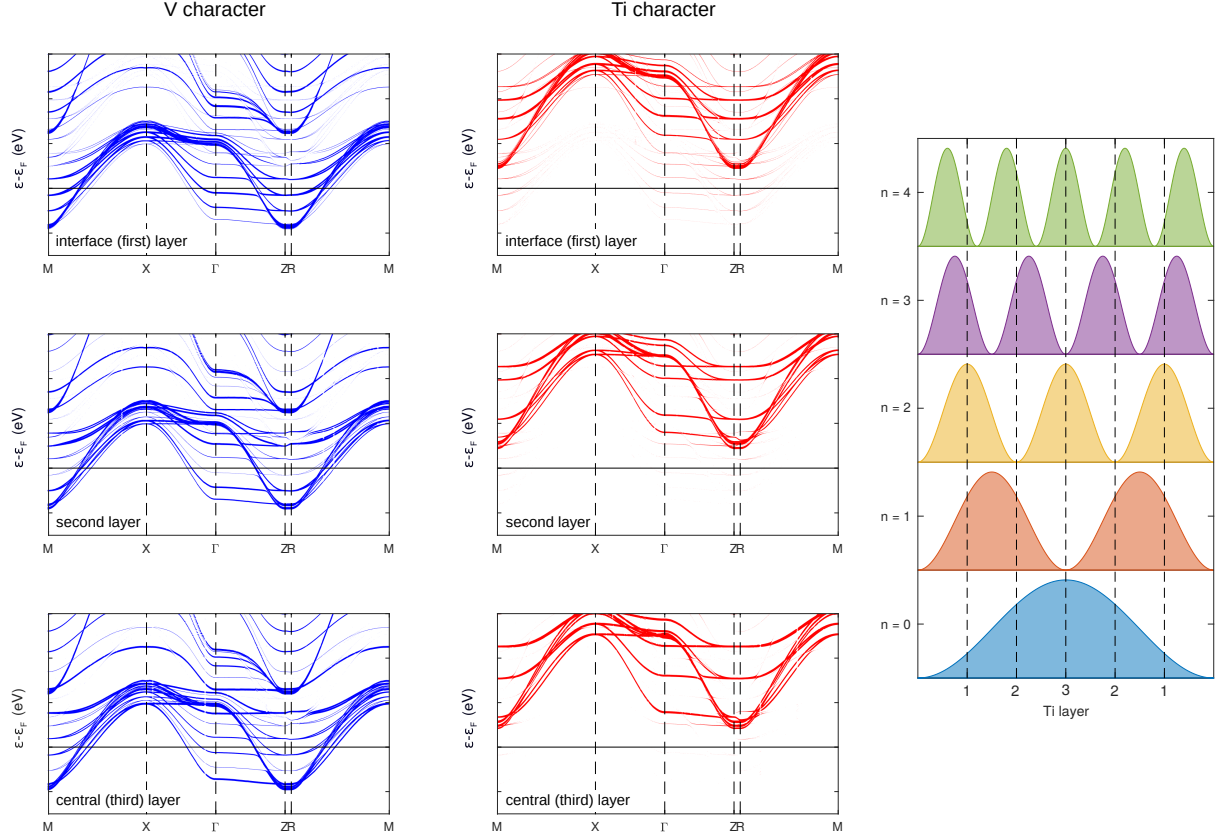


FIG. S4. The DFT V and Ti t_{2g} band characters of the 6:5 superlattice (SL). The thickness of the lines indicates the total character of each V (left) and Ti (right) site. The top row shows the band characters at the interface, while the bottom row shows the character in the center of the each layer. On the right, a schematic illustration of the real-space probability distribution of the quantized subbands in the out-of-plane direction of the SrTiO₃ layers is shown. The edge of the box does not coincide with the interface Ti ion or its neighboring SrO layer due to the finite phase accumulated at the interface.

The Ti band characters shed light on the broadening of the Ti bands in the DFT+DMFT calculations shown in Fig. 3 of the main manuscript. As above, the central Ti ion contributes strongly to the Ti $n = 0$ and $n = 2$ subbands. On the other hand, the interfacial Ti ion contributes significantly to the Ti $n = 1, 2$ and 3 subbands, with the largest contribution to the Ti $n = 2$ subband. The interfacial Ti ion mixes most strongly with the V orbitals, which are the correlated orbitals in the subsequent DMFT cycle. This demonstrates how the spatial penetration of the Ti $n = 1$ and $n = 2$ subbands into the correlated SrVO₃ layers leads to substantial broadening of these subbands in the subsequent DMFT cycle. In contrast, the Ti $n = 0$ subband is spatially deep within the SrTiO₃ layer and does not feel the effects of the correlated SrVO₃ orbitals very strongly, remaining reasonably sharp even in the insulating phase [Fig. 3(j) of the main manuscript].

QUANTIZED TIGHT-BINDING MODEL

Bulk tight-binding bands

The tight-binding (TB) model was constructed up to 12th nearest neighbors, consisting of 24 hopping terms, t_i , up to $[l, m, n] = [2, 2, 2]$. For the xy band the TB dispersion, ϵ_{xy} , is given by,

$$\epsilon_{xy} = E_{xy}^0 + \sum_{lmn} t_{xy}^{lmn} \cos(lk_x + mk_y + nk_z), \quad (1)$$

where the band energy, E_{xy}^0 , corresponds to the crystal field energy. Since the purpose of our model is to accurately describe the bulk 3D DFT band structure, we do not attempt to analyze individual parameters, as has been done before [5]. Although terms corresponding to the 5th nearest neighbor and higher had a magnitude of less than 10 meV, these terms were found to be necessary to adequately describe the FP-LAPW band structure. After fitting this model to the bulk LDA band structure in the full cubic Brillouin zone, we find the r.m.s.

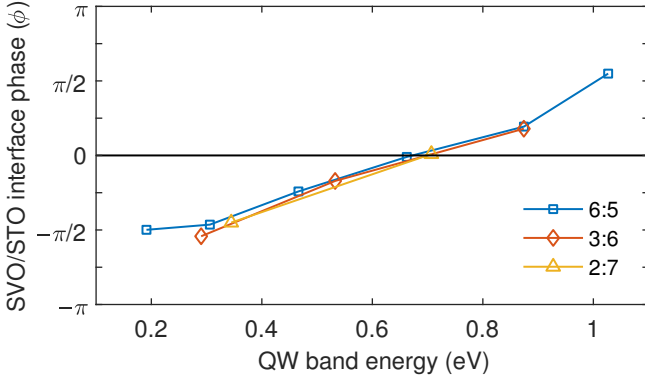


FIG. S5. The phase shift at the SrVO₃/SrTiO₃ interface for each quantized state in the SLs (note $\phi_n = \delta_n/2$ is shown), shown against the mean band energy.

difference is less than 11 meV, with a maximum difference of 70 meV.

Quantum confinement

In order to account for the effects of quantum confinement of the V 3d electrons in the SrVO₃ layers, we apply the Bohr-Sommerfeld phase accumulation model [6],

$$2k_z^n(E)L + \delta(E) = 2\pi n, \quad (2)$$

where $n = 0, 1, 2, \dots$ is the quantum number, $2k_z^n(E)L$ is the total phase accumulated in traveling through the SrVO₃ layer and back, $k_z^n(E)$ is the quantized out-of-plane wavevector, $L = mc$ is the SrVO₃ layer thickness (m and c are the number of SrVO₃ layers and c -axis lattice parameter of the SrVO₃ layers, respectively). $\delta(E)$ is the total phase acquired due to reflection at both SrVO₃/SrTiO₃ interfaces. For asymmetric quantum wells, e.g. thin overlayers with a vacuum interface, $\delta = \phi_1 + \phi_2$ is composed of different individual phase shifts at each reflection; in our case of symmetric barriers, $\delta = 2\phi$, where ϕ is the phase at a single SrVO₃/SrTiO₃ interface. In general, $\delta = \delta(E)$ is explicitly dependent on the energy of the confined state. However, in order to simplify the fitting, and avoid unnecessary degrees of freedom, we instead implicitly include the energy dependence through different phases for each quantum number, $\delta = \delta_n$. With this, the quantization condition reduces to,

$$k_z^n = \frac{2\pi n - \delta_n}{2mc}, \quad (3)$$

from which the quantized TB dispersion, $E_n(k_x, k_y, k_z^n)$, may be evaluated.

Full quantization parameters

For each SL, four parameters were fitted to describe the “intrinsic” band structure, and n parameters described the con-

finied bands. The quantized TB dispersion was fitted to the FP-LAPW ELK band structure of the SLs. The four intrinsic parameters consist of band centers (E_i^0 in Eqn. 1) and band widths for the xy and $xz(yz)$ bands. The band width parameter, W_i , is a multiplicative factor to the hopping terms, t_i (the hopping terms themselves were fixed to the cubic bulk parameters determined above, effectively fixing the shape of the band). In addition to the intrinsic parameters, the phase shifts for each confined state, δ_n , were also fitted. The fitted phases are shown in Fig. S5 against the mean energy of each state, and closely follow the same roughly linear relationship with energy for all SLs.

The results of fitting the FP-LAPW bands to the quantized TB model are shown in Table I, separated into contributions from the underlying bulk “intrinsic” bands and after quantizing these bands. An example of the fitted band structure is shown in Fig. 1 of the main paper for the 2:7 SL. Since its wavefunction is perpendicular to the quantization axis, the xy bandwidth is hardly affected by confinement, but the $xz(yz)$ bands are significantly narrowed compared with their intrinsic (bulk-like) counterparts. The confinement leads to the preferential filling of the quantized $xz(yz)$ out-of-plane bands as their k_z dispersion is suppressed and they become 1D-like, which also pulls the Fermi level down slightly.

We note that confinement alone is capable of reproducing the SL band structure to a large extent, correctly describing the narrowing of the quantized bandwidth and its variation with SrVO₃ layer thickness. This has been checked by restricting the “intrinsic” bands in the fit to the bulk bands (i.e. setting E_i^0 and W_i to the bulk ones). This provides additional support that the band narrowing that eventually drives the MIT is primarily due to quantization effects rather than crystal field (CF) effects.

DYNAMICAL MEAN-FIELD THEORY CALCULATIONS

The output from the ELK DFT calculation was imported to the TRIQS library [7] via an in-house interface with the dmftproj [8] application. As in the literature [9–11], only the V t_{2g} bands were projected (using Wannier projectors) [12] to construct the LDA Hamiltonian in Wannier space. These projectors were constructed in the following correlated energy

SL	CF splitting (meV)	Intrinsic			Quantized bands		
		W_{xy}	W_{yz}	anis.	W_{xy}	W_{yz}	anis.
6:5	33	0.966	0.959	0.993	0.950	0.900	0.948
3:6	40	0.971	0.960	0.989	0.935	0.798	0.853
2:7	51	0.963	0.952	0.988	0.911	0.713	0.782

TABLE I. Results of fitting the FP-LAPW ELK bands to a quantized tight-binding model. The crystal field (CF) splitting is the energy difference, $E_{yz}^0 - E_{xy}^0$. The bandwidth (relative to bulk SrVO₃), W_i , of the xy and yz bands are shown for both intrinsic bands (before quantization) and for the quantized bands, alongside their anisotropy (W_{yz}/W_{xy}).

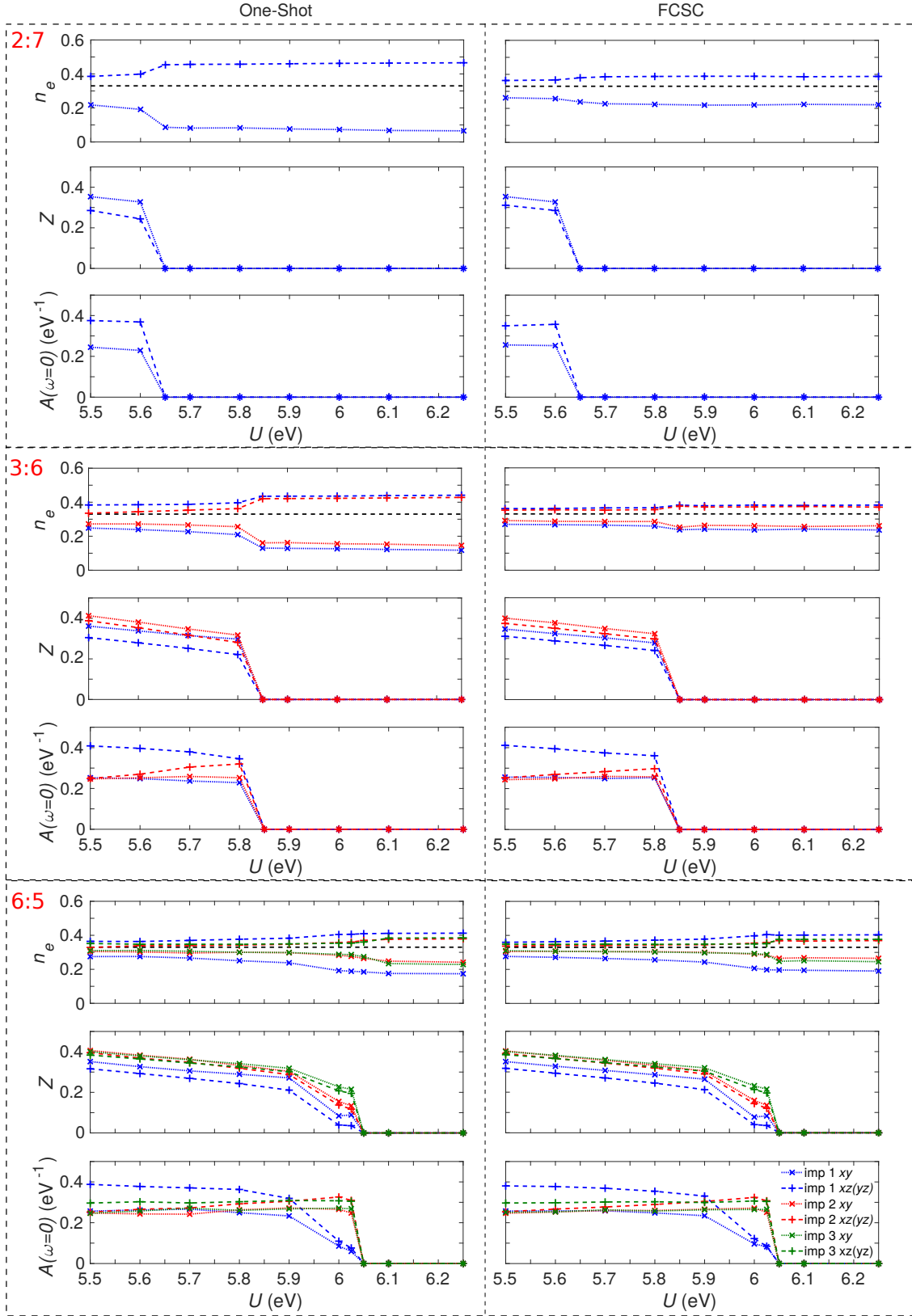


FIG. S6. The effect of U on the orbital charge n_e (top), quasiparticle residue Z (middle) and the spectral function around the Fermi level (bottom) for each SL one-shot and fully charge self-consistent (FCSC) DFT+DMFT calculation. The dashed line represents the bulk degenerate orbital charge.

windows: 2:7 SL: $[-1.36, 2.0]$ eV, 3:6 SL: $[-1.29, 2.0]$ eV, 6:5 SL: $[-1.29, 2.0]$ eV and bulk: $[-1.50, 1.90]$ eV. These

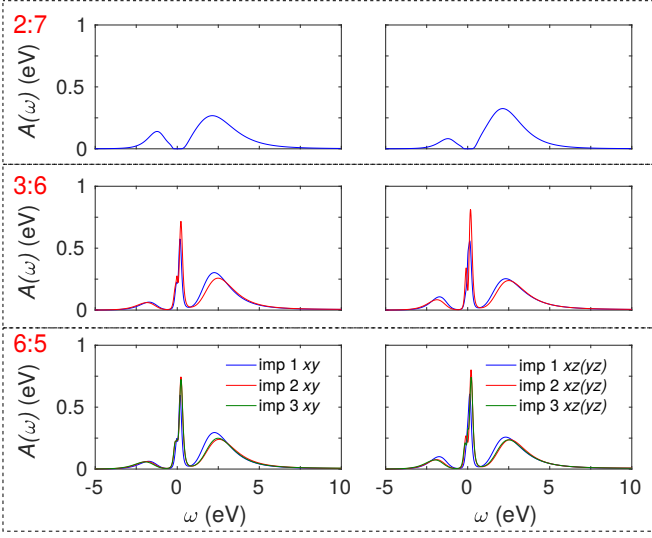


FIG. S7. Spectral functions of the 2:7 (top), 3:6 (middle) and 6:5 (bottom) SLs from fully charge self-consistent calculations, showing xy (left) and $xz(yz)$ (right) orbitals. The spectra of the insulating 2:7 SL have been shifted such that the Fermi level lies at the center of the band gap of the xy spectrum.

windows were constructed such that all of the V t_{2g} bands are included and the valence charge above the lower bound, corresponding to the charge in the V t_{2g} orbitals, is equal to 1 per V impurity. Each DMFT cycle calculation used 84×10^6 Monte Carlo sweeps.

In order to avoid potential complications from the ill-posed problem of analytic continuation, quantities were determined from the Green's function and self-energy on the imaginary time (τ) or frequency axis as much as possible. The charge of each orbital (n_e) was determined by,

$$n_e = \sum_n G(i\omega_n) e^{i\omega_n 0^+} \quad (4)$$

within the TRIQS library. As there is negligible inter orbital-orbital overlap on the impurity, n_e is diagonal. The spectral function at the Fermi level, $A(\omega = 0)$, is an averaged quantity over a frequency window approximately equal to T [9]. Here, $A(\omega = 0)$ is determined directly from the imaginary time Green's function by,

$$A(\omega = 0) = \frac{\beta G(\tau = \frac{1}{2}\beta)}{\pi}, \quad (5)$$

where β is the inverse temperature in natural units. The value of QP residue Z was determined by

$$Z = \left(1 - \frac{\partial \text{Im}[\Sigma(i\omega_n)]}{\partial i\omega_n} \bigg|_{i\omega_n \rightarrow 0^+} \right)^{-1}, \quad (6)$$

where the Z is evaluated from the differential of the imaginary part of the Matsubara self-energy at $i\omega_n \rightarrow 0^+$. For U values

far from the Fermi liquid regime (namely for the 6:5 Z values close to the MIT), the Z values were approximated by using the differential of the interpolated self-energies at $i\omega_n = 0$. There are two ways to realize the insulating solution. First, by a divergence in $\text{Im}[\Sigma(i\omega_n)]$, which comes naturally with $Z = 0$. Second, the combination of the $\text{Re}[\Sigma(i\omega_n)]$ and the chemical potential might move the pole position outside of the non-interacting bandwidth, meaning that no QP peak is possible in the Green's function. In the latter case, we have $A(\omega = 0)$ vanishing with non-diverging $\text{Im}[\Sigma(i\omega_n)]$. In that case, that we also see here, we set Z to zero manually. From this, the MIT U value (U_{MIT}) is defined as the lowest U value in which $A(\omega = 0) = 0$.

The spectral functions, $A(\omega)$, for each impurity were calculated from $G(\tau)$ using the *LineFitAnalyzer* technique of the maximum entropy analytic continuation method implemented within the *MaxEnt* application of TRIQS [13]. The k -resolved spectral functions $A(\mathbf{k}, \omega)$ were calculated from the analytically continued self-energy.

The effective and correlation subband mass enhancement factors, $1/Z_\nu$ and $1/Z_\nu^c$, were calculated from the ratios of the Fermi velocities using

$$Z_\nu^c = \frac{v_F^c}{v_F^{\text{QTB}}} \quad (7)$$

and

$$Z_\nu = \frac{v_F^c}{v_F^i}. \quad (8)$$

Here, the Fermi velocities were determined from the gradient of the linearly expanded band dispersions along M-X around k_F of the DFT+DMFT subbands (v_F^c), the quantized bands from QTB (v_F^{QTB}) and the intrinsic (bulk-like) TB bands (v_F^i). The intrinsic bands were used as they incorporate the effect of renormalization due to strain. Therefore, Z_ν^c and Z_ν describe the effect of renormalization from correlations and the combination of correlations and confinement (band) effects respectively.

The DFT+DMFT subband energy centers, $E_{\nu,\mathbf{k}}$, were calculated by using

$$E_{\nu,\mathbf{k}} = \epsilon_{\nu,\mathbf{k}} - \mu + \text{Re}[\Sigma_\nu(\mathbf{k}, \omega = E_{\nu,\mathbf{k}})], \quad (9)$$

where $\epsilon_{\nu,\mathbf{k}}$ is the DFT energy, μ is the chemical potential and $\text{Re}[\Sigma_\nu(\mathbf{k}, \omega)]$ is the real part of the diagonal upfolded self-energy elements on the real frequency axis. The QP lifetime in the inset of Fig. 4 of the main manuscript was determined from the inverse imaginary part of the analytically continued upfolded self-energy. Finally, the subband energies at the Γ high symmetry point in Fig. 4 of the main manuscript were determined from Eqn. 9.

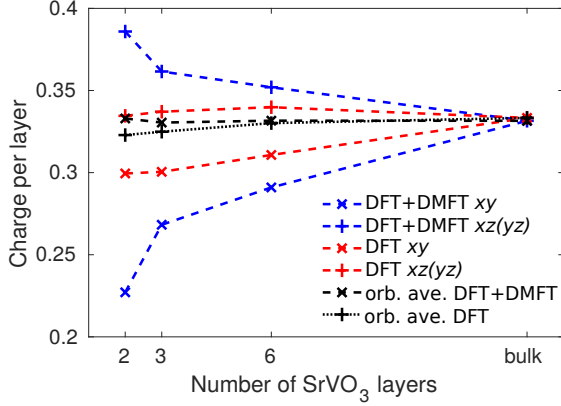


FIG. S8. The averaged orbital charge over all layers from the DFT and DFT+DMFT Wannier V xy and $xz(yz)$ orbitals for each SL and bulk. This includes charges from DFT, DFT+DMFT and average orbital charge per layer (orb. ave.) for each SL and bulk.

One-shot and FCSC DFT+DMFT results

The main manuscript presents fully charge self-consistent (FCSC) DFT+DMFT calculations. Here, we present the results of one-shot (OS) DFT+DMFT for comparison. Overall, charge self-consistency slightly adjusts some details of the results, but the main conclusions of our study are already present in one-shot calculations.

Figure S6 shows the U -dependent MIT for each SL and different DFT+DMFT methods. The behavior of the OS and FCSC calculations is very similar, exhibiting a similar U_{MIT} with similar characteristics, e.g. $A(\omega = 0)$ and Z . Some differences are observed in the orbital polarization between the two methods, whereby the polarization is somewhat suppressed in the FCSC calculation compared with OS. This behavior, most notable for the 2:7 SL, is consistent with other studies [10, 11, 14], and is caused by the charge redistribution with the rest of the system at the DFT stage. This trend from 2:7 to bulk is also seen in Fig. S9 for the orbitally-averaged values of Z , where there are some differences in \bar{Z} for the 2:7 SL between OS and FCSC, but the bulk values are very similar.

An important note to make about Fig. S6 is that Z at the interface (imp 1) for the $xz(yz)$ orbitals tends to zero first for each SL. This suggests that the weight from the $xz(yz)$ QP peak depletes first. Therefore, when the interface $xz(yz)$ QP state has been fully depleted, this causes the SL to transition into the insulating state. From this, the interface between the oxides has a strong influence on the MIT. The $A(\omega = 0)$ for imp 1 of the 6:5 also tends to zero which strengthens the argument for at least that SL.

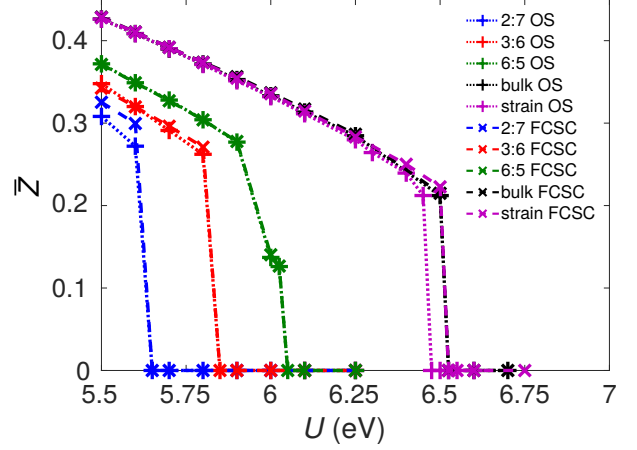


FIG. S9. The comparison of the orbitally-averaged quasiparticle residue, \bar{Z} , between the one-shot (OS and fully charge self-consistent (FCSC) DFT+DMFT methods. The plot lines are guides to the eye.

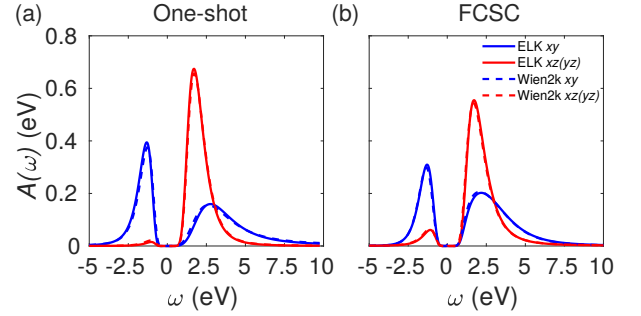


FIG. S10. The orbital $A(\omega)$ comparisons between the one shot and fully charge self consistent (FCSC) DFT+DMFT methods from different input DFT codes for mono layer SrVO_3 .

OTHER SIGNIFICANT SL FCSC RESULTS

Fig. S7 shows the $A(\omega)$ of each correlated impurity orbital in each SL at $U = 5.7$ eV (the value used in the theoretical-experimental comparisons). It is evident that the 2:7 is insulating and the 3:6 and 6:5 is metallic from the absence/presence of the QP peak at the Fermi level. There are sharp features in the QP peaks around the Fermi level for the 3:6 and 6:5 SLs. These features are often attributed to spurious noise from the analytic continuation procedure, however, it may not be the case here due to the quantized bands being present around the Fermi level. The peak position of the Hubbard bands (notably the UHB) are closer in energy to the Fermi level for the interface layer (impurity 1) compared to the other layers for the 3:6 and 6:5. This is another indication that the interface layer is more correlated compared to the other layers.

The splitting of the orbital degeneracy strongly effects the polarization of the orbital charge as shown in Fig. S8. It is interesting to note that the reduction of the number of layers sig-

nificantly increases the charge in the $xz(yz)$ orbitals, which appear to tend to half filling (whereas the xy orbitals are tending towards zero charge). This is a likely consequence of these orbitals trying to reduce the potential energy, analogous to what is seen in the previous mono layer calculations. The reduction in the orbitally-averaged DFT charge with lower SrVO_3 layers is likely due to hybridization with Ti at the interface.

Elk-TRIQS interface test: monolayer SrVO_3

The results presented used an in-house interface between ELK and TRIQS, so this section presents comparison results between ELK and Wien2k inputs into TRIQS to show that the interface works for a similar system, namely monolayer SrVO_3 . The monolayer SrVO_3 calculation was set up in the same way and using the same parameters as in Ref. 11. Figure S10 shows the comparison between $A(\omega)$ calculated from the different DFT code inputs. This comparison shows excellent agreement between the different inputs for the different DFT+DMFT methods. This test shows that the interface used between Elk and TRIQS is able to reliably perform DFT+DMFT calculations.

EFFECTS OF STRAIN

We performed volume conserving strain calculations on bulk SrVO_3 to investigate the effect of CF has on the MIT while the bandwidths of the t_{2g} orbitals are approximately unchanged. Compressive strain of 1% was applied along the c -axis; the other axes were tensively strained to conserve volume compared with the bulk. This strain was chosen to yield a CF splitting of 53 meV, slightly larger than but comparable to the CF splitting of the 2:7 SL. The strained FCSC U_{MIT} is approximately 6.525 eV, the same as for the bulk. The OS strained calculation had a slightly lower U_{MIT} of 6.475 eV. Due to the small change on U_{MIT} , the CF splitting is insufficient to cause the MIT in these SLs.

- 10LT01 (2018).
- [2] J. Laverock, M. Gu, V. Jovic, J. W. Lu, S.A. Wolf, R. M. Qiao, W. Yang, and K.E. Smith, “Nano-engineering of electron correlation in oxide superlattices,” *Nano Futures* **1**, 031001 (2017).
 - [3] J. K. Dewhurst, S. Sharma, L. Nordström, F. Cricchio, O. Granas, and E. K. U. Gross, <http://elk.sourceforge.net/> (2019).
 - [4] K. Yoshimatsu, T. Okabe, H. Kumigashira, S. Okamoto, S. Aizaki, A. Fujimori, and M. Oshima, “Dimensional-crossover-driven metal-insulator transition in SrVO_3 ultrathin films,” *Phys. Rev. Lett.* **104**, 147601 (2010).
 - [5] A. Liebsch, “Surface versus Bulk Coulomb Correlations in Photoemission Spectra of SrVO_3 and CaVO_3 ,” *Phys. Rev. Lett.* **90**, 096401 (2003).
 - [6] T.-C. Chiang, “Photoemission studies of quantum well states in thin films,” *Surf. Sci. Rep.* **39**, 181 (2000).
 - [7] O. Parcollet, M. Ferrero, T. Ayril, H. Hafermann, I. Krivenko, L. Messio, and P. Seth, “TRIQS: A toolbox for research on interacting quantum systems,” *Comp. Phys. Commun.* **196**, 398 (2015).
 - [8] M. Aichhorn, L. Pourovskii, P. Seth, V. Vildosola, M. Zingl, O. E. Peil, X. Deng, J. Mravlje, G. J. Kraberger, C. Martins, M. Ferrero, and O. Parcollet, “TRIQS/DFTTools: A TRIQS application for ab initio calculations of correlated materials,” *Comp. Phys. Commun.* **204**, 200 (2016).
 - [9] Z. Zhong, M. Wallerberger, J. M. Tomczak, C. Taranto, N. Paragh, A. Toschi, G. Sangiovanni, and K. Held, “Electronics with Correlated Oxides: $\text{SrVO}_3/\text{SrTiO}_3$ as a Mott Transistor,” *Phys. Rev. Lett.* **114**, 246401 (2015).
 - [10] S. Bhandary, E. Assmann, M. Aichhorn, and K. Held, “Charge self-consistency in density functional theory combined with dynamical mean field theory: k -space reoccupation and orbital order,” *Phys. Rev. B* **94**, 155131 (2016).
 - [11] M. Schüler, O. E. Peil, G. J. Kraberger, R. Pordzik, M. Marsman, G. Kresse, T. O. Wehling, and M. Aichhorn, “Charge self-consistent many-body corrections using optimized projected localized orbitals,” *J. Phys.: Condens. Matter* **30**, 475901 (2018).
 - [12] M. Aichhorn, L. Pourovskii, V. Vildosola, M. Ferrero, O. Parcollet, T. Miyake, A. Georges, and S. Biermann, “Dynamical mean-field theory within an augmented plane-wave framework: Assessing electronic correlations in the iron pnictide LaFeAsO ,” *Phys. Rev. B* **80**, 085101 (2009).
 - [13] G. J. Kraberger and M. Zingl, <https://github.com/TRIQS/maxent> (2019).
 - [14] A. Hampel, S. Beck, and C. Ederer, “Charge self-consistency and double-counting in DFT+DMFT calculations for complex transition metal oxides,” *arXiv:1907.10339* (2019).

[1] M. Gu, S. A. Wolf, and J. Lu, “Transport phenomena in $\text{SrVO}_3/\text{SrTiO}_3$ superlattices,” *J. Phys. D: Appl. Phys.* **51**,